Confinement-Induced Resonances in Spherical Shell Traps

C. Moritz Carmesin[1,*] and Maxim A. Efremov[1,2]
[1]Institut für Quantenphysik and Center for Integrated Quantum Science and Technology (IQST), Universität Ulm, 89081 Ulm, Germany
[2]German Aerospace Center (DLR), Institute of Quantum Technologies, 89081 Ulm, Germany

(Received 6 December 2023; revised 8 May 2025; accepted 14 May 2025; published 17 June 2025)

The energy spectrum and corresponding wave functions of two bosonic particles confined in a spherically symmetric shell trap and interacting via a three-dimensional zero-range potential are computed. Confinement-induced resonances, originating entirely from the strong coupling of the relative and center-of-mass motions of the two particles, are identified as avoided crossings for certain values of the shell radius. By working close to the found resonances, these results offer a new way to control the atom-atom interaction in an atomic gas by tuning only the geometrical parameters of the shell.

DOI: 10.1103/hfyx-r11q

Introduction—Ultracold atomic bubbles are atomic quantum gases confined to closed two-dimensional (2D) surfaces like spherical or ellipsoidal shells. They have recently attracted significant interest as the best platform to probe fundamental concepts of few- and many-body quantum theory and statistical mechanics in curved manifolds [1,2]. Nowadays, there exist only two working schemes [3–5] for producing atomic shells in labs [6]. The first is using radio-frequency dressing [7–10] in a microgravity environment [11–15], resulting in ellipsoidal shells. The second scheme involves optically confined mixtures of two Bose-Einstein condensates (BEC) and either employs a magic laser wavelength [5,16], or combines microgravity [17] with Feshbach resonances [18,19], to tune the interspecies interaction. This yields spherical shells for one of the mixture components. The successful realizations of this novel topology have inspired many groups to reexamine many well-known phenomena, originally discovered for a flat geometry, but now in the case of quantum atomic bubbles. Many studies have explored the influence of curvature on Bose-Einstein condensation [20–24], the collective excitations in condensate shells [17,25–27], vortices [28–31], the Berezinskii-Kosterlitz-Thouless transition [32,33], and potential scattering of particles [34,35].

In these phenomena, the interaction between atoms, leading to nonlinear dynamics, plays a crucial role. However, for a limited number of atoms in a spherical shell, the density of atoms decreases rapidly as $1/r_0^2$ with increasing radius r_0 of the shell [36]. Therefore, for large thin shells, where we have an ideal curved manifold, the atom-atom interaction becomes negligible. Thus, to have the possibility to experimentally study any interaction-driven phenomenon on shells, one has to find a scheme to adjust the atom-atom interaction. Most importantly, such a scheme cannot be based on magnetic or optical fields, as they are already used to create a shell-shaped trap or to tune the repulsive interspecies interaction.

To address this problem, we propose and study in this Letter confinement-induced resonances (CIRs) as a reliable tool to tune the interaction between tightly confined atoms [37]. The use of CIRs provides an effective solution to a critical problem in the investigation of how curvature affects many physical phenomena, occurring in few- and many-body physics, statistical mechanics, and physical kinetics. This is due to the fact that in the presence of a confinement, the scattering properties [38–40] and the binding spectrum [41] of two atoms show remarkable changes compared to the confinement-free atoms. Here we show that in a spherically symmetric bubble many CIRs appear at certain r_0. To do this, we exactly compute the energy spectrum and the corresponding wave functions of two bosonic particles, which are confined in a *shell-shaped trap* and interact with each other via a *3D* s-wave zero-range potential characterized by the scattering length a_0. On this basis, we determine the position and width of the CIRs as a function of a_0 and r_0.

The found CIRs are identified as avoided crossings between a bound (molecular) state with excitation of the center-of-mass (c.m.) motion and a trap (nonmolecular) state without c.m. excitation, as well as between two trap states. These resonances originate entirely from the strong coupling between the c.m. and relative degrees of freedom of the two confined particles. Similar CIRs occur in a system of two identical atoms in an anharmonic trap [42,43], or with

*Contact author: moritz.carmesin@uni-ulm.de

heteronucler atoms in a harmonic confinement [44–46]. Consequently, a slow change of r_0 around a bound-trap CIR results in the formation of a two-particle molecule, mediated by the confinement and without requiring a third particle. This is because only the total energy of two trapped particles is fixed and can be redistributed between the energies of the c.m. and relative degrees of freedom, as well as their coupling energy. Moreover, the confinement-supported formation of molecules is a basic loss mechanism and provides an experimental scheme to observe the found bound-trap CIRs and thus to explore the stability of the atomic bubble. The found trap-trap CIRs are of great importance for accurately modeling the effective atom-atom interaction and the corresponding nonlinear term in the Gross-Pitaevskii equation, while performing a dimensional reduction of BEC dynamics from 3D to 2D curved manifolds [24].

Confinement-induced resonances—The emergence of CIRs can be easily understood in terms of configurations. This term refers here to the spatial geometry of the two-particle wave function, induced not only by the interaction and confinement, but most importantly, by the distribution of energy among the different degrees of freedom. This becomes visible as a varying number of nodes in each degree of freedom.

To illustrate this phenomenon, Fig. 1 presents the general picture of a CIR. For a certain interval of the system parameter, in our case it is r_0, the energy of the adiabatic state $|\alpha\rangle$ comes close to the one of the state $|\beta\rangle$. For smaller r_0, $|\alpha\rangle$ represents configuration I (red color) whereas $|\beta\rangle$ the different configuration II (blue). As an example, at a bound-trap CIR, the configuration I has essentially the form of two noninteracting particles, each of them is in the ground state of the trap, whereas the configuration II describes strong localization in the relative degrees of freedom and excitation in the c.m. ones. At the avoided crossing, the configurations mix up, associated with a redistribution of the total energy of the state between different coupled degrees of freedom. For slightly larger values of r_0, the adiabatic states have interchanged their configurations, i. e. $|\alpha\rangle$ now features the configuration II and vice versa.

Generally, a CIR occurs when (i) the energies of two different configurations approach each other or cross, cf. the dotted lines in Fig. 1, and (ii) the confinement causes a coupling of these configurations. This coupling induces avoided crossings in the energy spectrum of the adiabatic eigenstates, so that the diabatic states—each corresponding to one of the involved configurations—interact strongly.

Two particles in a spherical shell trap—We consider two identical bosons of mass m, which are trapped in a shell potential [26] modeled as a spherically symmetric shifted harmonic oscillator $V_0(\boldsymbol{r}_i) = \frac{1}{2}m\omega^2(|\boldsymbol{r}_i| - r_0)^2$, where $i = 1$ or 2, with the trap frequency ω and the shift r_0 of the potential minimum. The width of the trapping potential is thus characterized by the oscillator length $a_{\mathrm{ho}} = \sqrt{\hbar/(m\omega)}$.

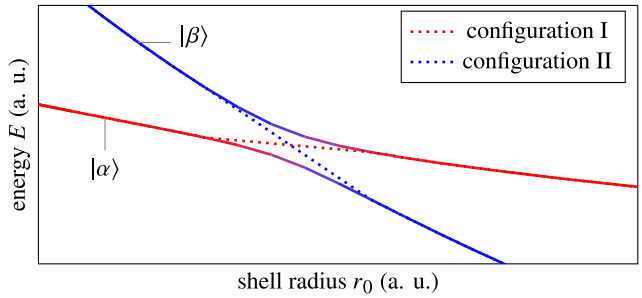

FIG. 1. Energy level scheme at a CIR resulting from the coupling of two diabatic states (dotted lines), pertaining to the different configurations I (red) and II (blue). The resulting adiabatic states $|\alpha\rangle$ and $|\beta\rangle$ (solid lines) avoid crossing and allow the adiabatic transition from one configuration into the other by tuning the shell radius. The adiabatic states are colored according to their overlap with the diabatic states by adjusting the transparency of each color: full opacity means full overlap while transparency indicates decreased overlap.

Instead of the commonly used Fermi-Huang 3D pseudopotential we equivalently model the s-wave interparticle interaction by the Bethe-Peierls boundary condition [47] for the two-particle wave function Ψ:

$$\lim_{r_1 \to r_2} \left\{ \frac{\partial[|\boldsymbol{r}_1 - \boldsymbol{r}_2|\Psi(\boldsymbol{r}_1, \boldsymbol{r}_2)]}{\partial|\boldsymbol{r}_1 - \boldsymbol{r}_2|} + \frac{|\boldsymbol{r}_1 - \boldsymbol{r}_2|}{a_0}\Psi(\boldsymbol{r}_1, \boldsymbol{r}_2) \right\} = 0 \tag{1a}$$

for partial waves with zero relative angular momentum, $\ell = 0$, and

$$\lim_{r_1 \to r_2} |\boldsymbol{r}_1 - \boldsymbol{r}_2|\Psi(\boldsymbol{r}_1, \boldsymbol{r}_2) = 0 \tag{1b}$$

for partial waves with the relative angular momentum $\ell > 0$.

In the case of an ordinary spherically symmetric harmonic confinement, that is the case of $r_0 = 0$, both the Hamiltonian

$$\hat{H} = -\frac{\hbar^2}{2m}(\Delta_{\boldsymbol{r}_1} + \Delta_{\boldsymbol{r}_2}) + V_0(\boldsymbol{r}_1) + V_0(\boldsymbol{r}_2) \tag{2}$$

of our system and the boundary conditions, Eqs. (1a) and (1b), are separable in terms of the relative $\boldsymbol{r} = \boldsymbol{r}_1 - \boldsymbol{r}_2$ and c.m. $\boldsymbol{R} = \frac{1}{2}(\boldsymbol{r}_1 + \boldsymbol{r}_2)$ coordinates and the two-particle energy spectrum can be derived analytically [41]. Here $\Delta_{\boldsymbol{r}}$ denotes the 3D Laplace operator. In this Letter, we however consider the case of $r_0 > 0$, giving rise to nonseparability of the Hamiltonian in terms of the $\boldsymbol{r}$ and $\boldsymbol{R}$ coordinates.

To solve exactly the resulting six-dimensional stationary Schrödinger equation $\hat{H}\Psi = E\Psi$ for the two-particle wave function Ψ with the corresponding two-particle energy E, we perform numerical computations in terms of the relative and c.m. coordinates by applying a two-step approach [48]. First, we compute a set of basis functions, consisting of the c.m. wave functions, being the eigenfunctions of the shifted

radial harmonic oscillator with Dirichlet boundary condition, and the relative wave functions, being the eigenfunctions of a radially symmetric harmonic oscillator, but obeying the boundary conditions, Eqs. (1a) and (1b). Second, we represent $\hat{H}$ in terms of these radial basis functions, combined with spherical harmonics for the angular degrees of freedom. The resulting matrix is finally diagonalized.

To interpret correctly the solutions featuring a strong coupling between c.m. and relative motions, it is essential to work within the coordinates where the coupling is minimal, allowing for an effective reduction of the dimensionality of the problem. For our physical system, this is achieved with the hyperspherical coordinates [49]: the hyperradius $\xi = \sqrt{\frac{1}{2}r^2 + 2R^2}$, the hyperangle $\chi = \arctan(r/2R)$, the spherical angles θ and ϕ of $\boldsymbol{r}$, as well as Θ and Φ of $\boldsymbol{R}$. In the limit of a thin shell, $r_0/a_{\mathrm{ho}} \to \infty$, χ converges to $\theta_{12}/2$, with θ_{12} being the angle between $\boldsymbol{r}_1$ and $\boldsymbol{r}_2$. The explicit expressions of Eqs. (1a), (1b) and (2) in the hyperspherical coordinates, as well as the details of the subsequently employed approximations are presented in the appendices. Working with these hyperspherical coordinates, we can approximately separate the angular variables, θ, ϕ, Θ, and Φ, from ξ and χ. Furthermore, by considering the hyperradius ξ as an adiabatic coordinate [48], we can obtain approximately the hyperangular eigenfunctions $V_{n_\chi L\ell,\xi}(\chi)$ and the corresponding eigenvalues $\lambda(n_\chi, L, \ell; \xi)$. Here L and ℓ are eigenvalues of the angular momentum operator of c.m. $\hat{\boldsymbol{L}}$ and relative $\widehat{\boldsymbol{\ell}}$ motions, respectively, and n_χ denotes the number of nodes of the wave function $V_{n_\chi L\ell,\xi}(\chi)$ along the χ direction. These enable one to find the hyperradial wave functions $U_{n_\xi n_\chi L\ell}(\xi)$ and the two-particle energies $E_{n_\xi n_\chi L\ell}$, where n_ξ is the number of nodes of $U_{n_\xi n_\chi L\ell}(\xi)$ along the ξ direction.

Energy spectrum—We note that for $r_0 > 0$ both operators $\hat{\boldsymbol{L}}$ and $\widehat{\boldsymbol{\ell}}$ do not commute with the Hamiltonian of the system including the Fermi-Huang pseudopotential, or the corresponding boundary conditions Eqs. (1a) and (1b). However, the operator of the total angular momentum $\hat{\boldsymbol{J}} = \hat{\boldsymbol{L}} + \widehat{\boldsymbol{\ell}}$ does commute and therefore provides the quantum numbers $\{J, M_J\}$.

We exemplarily consider two-particle states with $J = 0$ and $M_J = 0$. For $a_0 = 0.53a_{\mathrm{ho}}$, we present in the upper panel of Fig. 2 by solid lines the dependence of the exactly obtained two-particle energies E_n on the shell radius r_0 [48]. Note that at $r_0 = 0$ the displayed energies $E_n(0)$ correspond to two-particle states with $L = 0$ and $\ell = 0$, as at $r_0 = 0$ there is no coupling between the c.m. and relative motion, and hence $\hat{\boldsymbol{L}}$ and $\widehat{\boldsymbol{\ell}}$ define the quantum numbers L and ℓ. For comparison, we also display in the upper panel of Fig. 2 by dotted lines the energies $E_{n_\xi n_\chi 00}(r_0) \equiv E_{n_\xi n_\chi}(r_0)$ of the approximate states $|n_\xi n_\chi 00\rangle$, where the

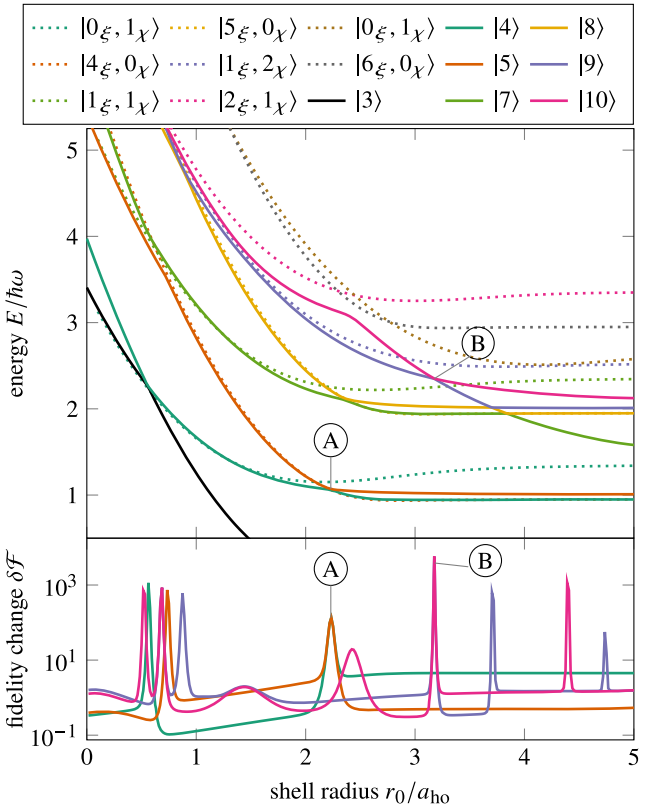

FIG. 2. The exact E_n (solid) and approximated $E_{n_\xi n_\chi}$ (dotted) two-particle energies (upper panel) and fidelity change $\delta\mathcal{F}_n$ (lower panel) as functions of r_0, for $a_0 = 0.53a_{\mathrm{ho}}$ and selected low energy states with $J = 0$ and $M_J = 0$. The two marked ACs Ⓐ: $|0_\xi 1_\chi\rangle$ (dark green) with $|4_\xi 0_\chi\rangle$ (orange), and Ⓑ: $|1_\xi 2_\chi\rangle$ (purple) with $|0_\xi 4_\chi\rangle$ (pink), are analyzed in detail. Note, AC Ⓐ is the energetically lowest one for the given a_0, [48] (Fig. S.1).

coupling of $\hat{\boldsymbol{L}}$ and $\widehat{\boldsymbol{\ell}}$ is neglected, as described in the appendices. The neglect of the coupling between $\hat{\boldsymbol{L}}$ and $\widehat{\boldsymbol{\ell}}$, determined by $\mathcal{V}_c$, Eq. (A4), is the dominant reason for the deviation of $E_{n_\xi n_\chi}(r_0)$ from $E_n(r_0)$.

Starting from $r_0 = 0$ the energies $E_{n_\xi n_\chi}(r_0)$ and $E_n(r_0)$ decrease rapidly with an increasing r_0 and then saturate. This is related to the transition from a 3D harmonic oscillator to an effectively 1D one for sufficiently large r_0, see appendices.

For intermediate r_0/a_{ho}, the energy spectrum displays many crossings and avoided crossings (AC). In general, their positions and widths are determined by both r_0 and a_0. To identify and quantify ACs, corresponding to CIRs [37,43], we analyze the fidelity change [50,51]

$$\delta\mathcal{F}_n(r_0) = \frac{1 - \langle n(r_0)|n(r_0 + \delta r_0)\rangle}{(\delta r_0/a_{\mathrm{ho}})^2} \tag{3}$$

of the exact eigenstates $|n\rangle$ as a function of r_0 for a given a_0. As clearly shown in the lower panel of Fig. 2, $\delta\mathcal{F}_n(r_0)$

exhibits peaks. When the peaks of the fidelity change $\delta\mathcal{F}_{n_1}$ of the state $|n_1\rangle$ and $\delta\mathcal{F}_{n_2}$ of the state $|n_2\rangle$ coincide, the constituent states of the AC are identified. These peaks determine the position and width of the ACs.

We emphasize that the avoided crossings are not restricted to the case $J = 0$ and $M_J = 0$. Indeed, they also occur in the two-particle energy spectrum for $J > 0$, see Ref. [48] (Fig. S1).

Structure of CIRs—We now consider in detail two kinds of avoided crossings, labeled by Ⓐ and Ⓑ in Fig. 2, respectively. To visualize the states involved at the ACs, we introduce the conditional probability density for the second particle of state $|n\rangle$

$$P^{(n)}_{2|1}(\varrho_2, z_2) = 2\pi\rho|\Psi_n(\rho_1 = 0, z_1 = r_0, \varrho_2, z_2)|^2, \quad (4)$$

given that the first particle is located at the potential minimum on the north pole. Exploiting the cylindrical symmetry of the selected states we have introduced the cylindrical coordinates (ϱ_i, z_i) for the ith particle, suppressing the dispensable azimuthal angles ϕ_i.

In Fig. 3(a), we display AC Ⓐ, which couples the diabatic states $|4_\xi 0_\chi\rangle$, shown in the top left inset by the density plot of $P^{(5)}_{2|1}(\varrho_2, z_2)$, and $|0_\xi 1_\chi\rangle$, shown in the bottom left inset by the density plot of $P^{(4)}_{2|1}(\varrho_2, z_2)$. The state $|4_\xi 0_\chi\rangle$ is tightly localized at the north pole, which can be attributed to a small relative distances r to the first particle. Actually, it resembles a bound state of two nontrapped particles with the characteristic exponential decay $\exp(-r/a_0)$. Such states correspond to *molecules on the shell* and only appear for positive a_0. They exhibit the molecular form only for small positive values of $a_0/a_{\rm ho}$, since otherwise the trap potential dominates. The state $|0_\xi 1_\chi\rangle$ of AC Ⓐ, possesses an approximate hyperradial symmetry, which is dictated by the trap structure and depicted in [48] (Fig. S2). The density plot in Fig. 3(a) also shows the approximate radial symmetry, while the hyperangular node appears as a node in the polar direction on the sphere. We denote such states as *trap states* of two particles. Avoided crossings, such as Ⓐ, describe an interplay between the molecular and trap states, are named as *bound-trap* CIRs.

The second kind of CIRs is exemplified by AC Ⓑ, Fig. 3(b). Here, the diabatic state $|0_\xi 4_\chi\rangle$, depicted in the top left inset by the density plot of $P^{(10)}_{2|1}(\varrho_2, z_2)$, is coupled to the state $|1_\xi 2_\chi\rangle$, depicted in the bottom left inset by the density plot of $P^{(9)}_{2|1}(\varrho_2, z_2)$. The number of hyperangular nodes is translated into the polar direction. The nodes of the hyperradial dimension appear as nodes in the spherical radius r_2. Since neither of the involved states is a molecular one, we call such ACs as *trap-trap* CIRs. Both kinds of resonances originate entirely from the strong coupling between the relative and c.m. degrees of freedom.

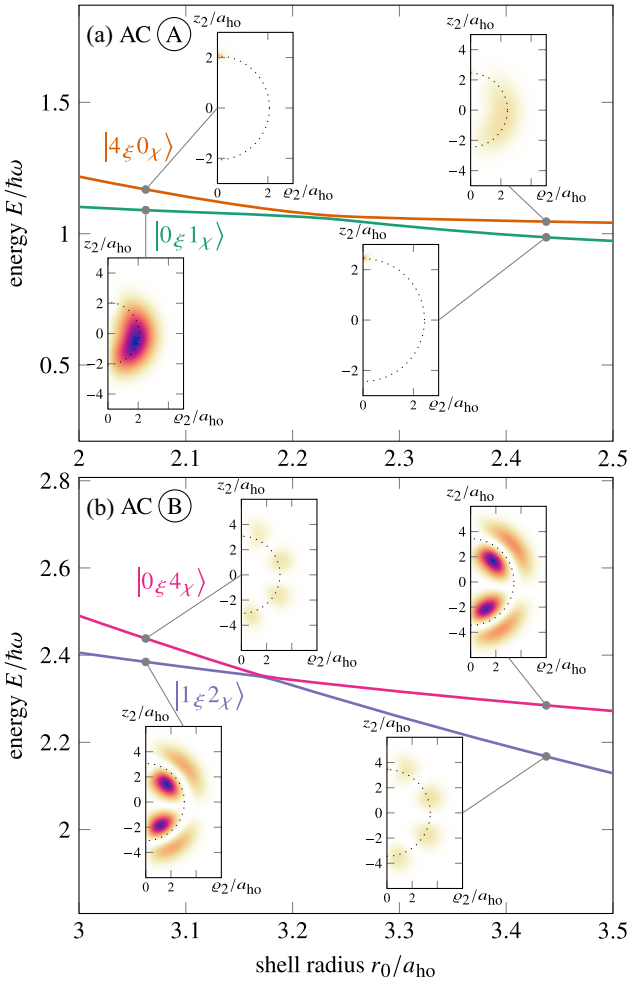

FIG. 3. Magnifications of the energy levels at AC Ⓐ and Ⓑ, Fig. 2. As insets, the conditional one-particle probability density $P_{2|1}(\varrho_2, z_2)$, Eq. (4), of the involved states before and after the avoided crossing are shown. See also Fig. S2 and Fig. S3 in [48] for density plots of the states as functions of r and R.

In Fig. 4 the positions of the AC Ⓐ and other two bound-trap CIRs (circles), as well as the AC Ⓑ (squares) are presented in the $r_0 - a_0$ parameter space. The positions of the bound-trap CIRs strongly depend on a_0, as the energy of the molecular state and hence the level spacing of the involved states are crucially determined by a_0. Consequently, a given trap state avoids crossing with the corresponding molecular state only in a small interval of a_0 and with increasing a_0 the position of this AC becomes shifted towards larger shell radii until it disappears. Note that close to the vanishing of an AC the curve in the $r_0 - a_0$ plane becomes nearly horizontal. This behavior is due to the fact that the involved energy levels become nearly parallel for large r_0, cf. Fig. 2. In contrast, the positions of trap-trap ACs like AC Ⓑ are nearly independent of a_0, as the shape and the energy level spacing of the involved trap states are essentially unaffected by a change of a_0.

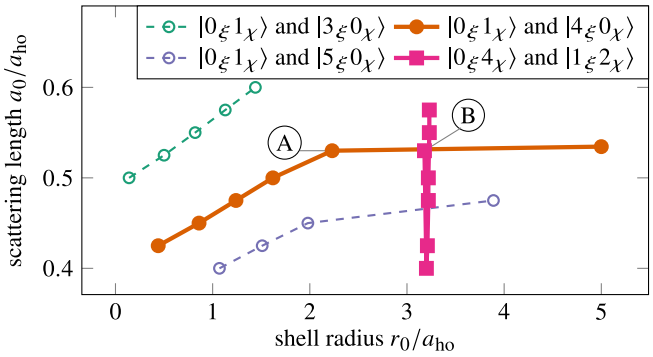

FIG. 4. Positions of selected avoided crossings of low-energy states with $J = 0$ and $M_J = 0$ in the $r_0 - a_0$ parameter space. The circles mark bound-trap ACs, similar to Ⓐ (orange), whereas the squares mark the trap-trap AC, like Ⓑ.

Summary and outlook—We have computed the energy spectrum and corresponding wave functions of two bosonic particles, which are confined in a spherically symmetric shell-shaped trap and interact with each other through a 3D s-wave zero-range potential. Further, we have identified two types of CIRs as avoided crossings between (i) a bound (molecular) state with strong localization in the relative coordinate and c.m. excitation and a trap (nonmolecular) state without c.m. excitation, and between (ii) two trap states. We have quantitatively determined the positions and widths of these resonances and shown clearly that they are induced by the strong coupling of the c.m. and relative motions of the two particles in the shell-shaped trap.

The found CIRs could be probed experimentally by observing losses in atomic bubbles. In fact, an adiabatic change of the shell radius r_0 around a bound-trap CIR drives the formation of molecules in the shell-shaped trap. The subsequent collisions of the formed molecules with each other, or with other atoms lead to the formation of tighter molecules and atoms with high kinetic energy, resulting in the loss of atoms from the trap. Depending on the actual realization of the quantum bubble, there are different schemes to scan the shell radius in a controllable way. In the case of the rf-dressing technique [7–10], this can be done by scanning the rf-detuning Δ, due to the fact that $r_0 \propto \sqrt{\Delta}$. For a shell potential generated with a two-species atomic mixture [5,17], the time-dependent shell radius can be realized, e.g., during free expansion. Additionally, it is of great interest to explore CIRs that occur in (i) ellipsoid-shaped traps, resulting usually from applying the rf-dressing scheme [7–10], and (ii) ring-shaped quantum gases [52]. The latter has useful applications in building compact and stable sensors for inertial and noninertial forces.

Acknowledgments—We thank A. Wolf for fruitful discussions and helpful suggestions. The authors acknowledge support by the state of Baden-Württemberg through bwHPC and the German Research Foundation (DFG) through Grant No. INST 40/575-1 FUGG (JUSTUS 2 cluster).

[1] A. Tononi and L. Salasnich, Low-dimensional quantum gases in curved geometries, Nat. Rev. Phys. **5**, 398 (2023).
[2] R. Dubessy and H. Perrin, Quantum gases in bubble traps, AVS Quantum Sci. **7**, 010501 (2025).
[3] R. A. Carollo, D. C. Aveline, B. Rhyno, S. Vishveshwara, C. Lannert, J. D. Murphree, E. R. Elliott, J. R. Williams, R. J. Thompson, and N. Lundblad, Observation of ultracold atomic bubbles in orbital microgravity, Nature (London) **606**, 281 (2022).
[4] Y. Guo, E. M. Gutierrez, D. Rey, T. Badr, A. Perrin, L. Longchambon, V. S. Bagnato, H. Perrin, and R. Dubessy, Expansion of a quantum gas in a shell trap, New J. Phys. **24**, 093040 (2022).
[5] F. Jia, Z. Huang, L. Qiu, R. Zhou, Y. Yan, and D. Wang, Expansion dynamics of a shell-shaped Bose-Einstein condensate, Phys. Rev. Lett. **129**, 243402 (2022).
[6] N. Lundblad, D. C. Aveline, A. Balaž, E. Bentine, N. P. Bigelow, P. Boegel, M. A. Efremov, N. Gaaloul, M. Meister, M. Olshanii, C. A. R. S. de Melo, A. Tononi, S. Vishveshwara, A. C. White, A. Wolf, and B. M. Garraway, Perspective on quantum bubbles in microgravity, Quantum Sci. Technol. **8**, 024003 (2023).
[7] O. Zobay and B. M. Garraway, Two-dimensional atom trapping in field-induced adiabatic potentials, Phys. Rev. Lett. **86**, 1195 (2001).
[8] O. Zobay and B. M. Garraway, Atom trapping and two-dimensional Bose-Einstein condensates in field-induced adiabatic potentials, Phys. Rev. A **69**, 023605 (2004).
[9] B. M. Garraway and H. Perrin, Recent developments in trapping and manipulation of atoms with adiabatic potentials, J. Phys. B **49**, 172001 (2016).
[10] H. Perrin and B. M. Garraway, *Chapter Four—Trapping Atoms with Radio Frequency Adiabatic Potentials*, edited by E. Arimondo, C. Lin, and S. F. Yelin, Advances In Atomic, Molecular, and Optical Physics (Academic Press, New York, 2017), Vol. 66, pp. 181–262.
[11] D. C. Aveline, J. R. Williams, E. R. Elliott, C. Dutenhoffer, J. R. Kellogg, J. M. Kohel, N. E. Lay, K. Oudrhiri, R. F. Shotwell, N. Yu, and R. J. Thompson, Observation of Bose-Einstein condensates in an earth-orbiting research lab, Nature (London) **582**, 193 (2020).
[12] N. J. Penley, C. P. Schafer, and J.-D. F. Bartoe, The international space station as a microgravity research platform, Acta Astron. **50**, 691 (2002).
[13] T. van Zoest *et al.*, Bose-Einstein condensation in microgravity, Science **328**, 1540 (2010).
[14] C. Lotz, Y. Wessarges, J. Hermsdorf, W. Ertmer, and L. Overmeyer, Novel active driven drop tower facility for microgravity experiments investigating production technologies on the example of substrate-free additive manufacturing, Adv. Space Res. **61**, 1967 (2018).
[15] K. Frye *et al.*, The Bose-Einstein condensate and cold atom laboratory, Eur. Phys. J. Quantum Technol. **8**, 1 (2021).

[16] M. Meister and A. Roura, Efficient matter-wave lensing of ultracold atomic mixtures, Quantum Sci. Technol. **8**, 024001 (2023).

[17] A. Wolf, P. Boegel, M. Meister, A. Balaž, N. Gaaloul, and M. A. Efremov, Shell-shaped Bose-Einstein condensates based on dual-species mixtures, Phys. Rev. A **106**, 013309 (2022).

[18] C. Chin, R. Grimm, P. Julienne, and E. Tiesinga, Feshbach resonances in ultracold gases, Rev. Mod. Phys. **82**, 1225 (2010).

[19] E. Timmermans, P. Tommasini, M. Hussein, and A. Kerman, Feshbach resonances in atomic Bose-Einstein condensates, Phys. Rep. **315**, 199 (1999).

[20] F. Dalfovo, S. Giorgini, L. P. Pitaevskii, and S. Stringari, Theory of Bose-Einstein condensation in trapped gases, Rev. Mod. Phys. **71**, 463 (1999).

[21] A. Tononi and L. Salasnich, Bose-Einstein condensation on the surface of a sphere, Phys. Rev. Lett. **123**, 160403 (2019).

[22] A. Tononi, F. Cinti, and L. Salasnich, Quantum bubbles in microgravity, Phys. Rev. Lett. **125**, 010402 (2020).

[23] B. Rhyno, N. Lundblad, D. C. Aveline, C. Lannert, and S. Vishveshwara, Thermodynamics in expanding shell-shaped Bose-Einstein condensates, Phys. Rev. A **104**, 063310 (2021).

[24] N. S. Móller, F. E. A. dos Santos, V. S. Bagnato, and A. Pelster, Bose–Einstein condensation on curved manifolds, New J. Phys. **22**, 063059 (2020).

[25] C. Lannert, T.-C. Wei, and S. Vishveshwara, Dynamics of condensate shells: Collective modes and expansion, Phys. Rev. A **75**, 013611 (2007).

[26] K. Sun, K. Padavić, F. Yang, S. Vishveshwara, and C. Lannert, Static and dynamic properties of shell-shaped condensates, Phys. Rev. A **98**, 013609 (2018).

[27] K. Padavić, K. Sun, C. Lannert, and S. Vishveshwara, Physics of hollow Bose-Einstein condensates, Europhys. Lett. **120**, 20004 (2018).

[28] A. L. Fetter, Rotating trapped Bose-Einstein condensates, Rev. Mod. Phys. **81**, 647 (2009).

[29] A. M. Turner, V. Vitelli, and D. R. Nelson, Vortices on curved surfaces, Rev. Mod. Phys. **82**, 1301 (2010).

[30] K. Padavić, K. Sun, C. Lannert, and S. Vishveshwara, Vortex-antivortex physics in shell-shaped Bose-Einstein condensates, Phys. Rev. A **102**, 043305 (2020).

[31] S. J. Bereta, M. A. Caracanhas, and A. L. Fetter, Superfluid vortex dynamics on a spherical film, Phys. Rev. A **103**, 053306 (2021).

[32] J. M. Kosterlitz, Kosterlitz-Thouless physics: A review of key issues, Rep. Prog. Phys. **79**, 026001 (2016).

[33] A. Tononi, A. Pelster, and L. Salasnich, Topological superfluid transition in bubble-trapped condensates, Phys. Rev. Res. **4**, 013122 (2022).

[34] J. Zhang and T.-L. Ho, Potential scattering on a spherical surface, J. Phys. B **51**, 115301 (2018).

[35] Z.-Y. Shi and H. Zhai, Emergent gauge field for a chiral bound state on curved surface, J. Phys. B **50**, 184006 (2017).

[36] P. Boegel, A. Wolf, M. Meister, and M. A. Efremov, Controlled expansion of shell-shaped Bose-Einstein condensates, Quantum Sci. Technol. **8**, 034001 (2023).

[37] V. Dunjko, M. G. Moore, T. Bergeman, and M. Olshanii, *Chapter 10—Confinement-Induced Resonances*, in *Advances in Atomic, Molecular, and Optical Physics*, edited by E. Arimondo, P. Berman, and C. Lin, Advances In Atomic, Molecular, and Optical Physics Vol. 60 (Academic Press, New York, 2011), pp. 461–510.

[38] M. Olshanii, Atomic scattering in the presence of an external confinement and a gas of impenetrable bosons, Phys. Rev. Lett. **81**, 938 (1998).

[39] T. Bergeman, M. G. Moore, and M. Olshanii, Atom-atom scattering under cylindrical harmonic confinement: Numerical and analytic studies of the confinement induced resonance, Phys. Rev. Lett. **91**, 163201 (2003).

[40] D. S. Petrov, M. Holzmann, and G. V. Shlyapnikov, Bose-Einstein condensation in quasi-2d trapped gases, Phys. Rev. Lett. **84**, 2551 (2000).

[41] T. Busch, B.-G. Englert, K. Rzażewski, and M. Wilkens, Two cold atoms in a harmonic trap, Found. Phys. **28**, 549 (1998).

[42] S. Sala, P.-I. Schneider, and A. Saenz, Inelastic confinement-induced resonances in low-dimensional quantum systems, Phys. Rev. Lett. **109**, 073201 (2012).

[43] S. Sala and A. Saenz, Theory of inelastic confinement-induced resonances due to the coupling of center-of-mass and relative motion, Phys. Rev. A **94**, 022713 (2016).

[44] V. Peano, M. Thorwart, C. Mora, and R. Egger, Confinement-induced resonances for a two-component ultracold atom gas in arbitrary quasi-one-dimensional traps, New J. Phys. **7**, 192 (2005).

[45] S. Grishkevich and A. Saenz, Influence of a tight isotropic harmonic trap on photoassociation in ultracold homonuclear alkali-metal gases, Phys. Rev. A **76**, 022704 (2007).

[46] V. S. Melezhik and P. Schmelcher, Quantum dynamics of resonant molecule formation in waveguides, New J. Phys. **11**, 073031 (2009).

[47] H. Bethe, R. Peierls, and D. R. Hartree, Quantum theory of the diplon, Proc. R. Soc. A **148**, 146 (1935).

[48] See Supplemental Material at http://link.aps.org/supplemental/10.1103/hfyx-r11q for a detailed description of the exact and approximate numerical solutions of the Schrödinger equation for the two-particle wave function, as well as the derivation of the asymptotic expansions for the two-particle energies.

[49] T. K. Das, *Hyperspherical Harmonics Expansion Techniques: Application to Problems in Physics*, 1st ed., Theoretical and Mathematical Physics (Springer-Verlag, Berlin, 2015).

[50] P. Plötz, M. Lubasch, and S. Wimberger, Detection of avoided crossings by fidelity, Physica (Amsterdam) **390A**, 1363 (2011).

[51] P. Plötz, Complex dynamics of ultracold atoms, Ph.D. thesis, Universität Heidelberg, 2010.

[52] L. Amico, D. Anderson, M. Boshier, J.-P. Brantut, L.-C. Kwek, A. Minguzzi, and W. von Klitzing, Colloquium: Atomtronic circuits: From many-body physics to quantum technologies, Rev. Mod. Phys. **94**, 041001 (2022).

[53] The neglect of $\mathcal{V}_c$ is valid only for $r_0 \lesssim 2a_{\mathrm{ho}}$. For increasing values of r_0, more and more terms of $\mathcal{V}_c$ have to be taken into account. For $r_0/a_{\mathrm{ho}} \to \infty$, however, the sum of $\mathcal{W}/\xi^2 + \mathcal{V}_c$ vanishes for particles exactly on the sphere with radius r_0.

End Matter

Appendix A: Hyperspherical representation—In hyperspherical coordinates the Hamiltonian, Eq. (2), reads

$$\hat{H} = -\frac{\hbar^2}{2m}\left(\frac{\partial^2}{\partial\xi^2} + \frac{5}{\xi}\frac{\partial}{\partial\xi} - \frac{\hat{\Lambda}^2}{\xi^2}\right) + \frac{m\omega^2}{2}(\xi - \xi_0)^2 + \mathcal{V}_c, \quad \text{(A1)}$$

where $\xi_0 = \sqrt{2}r_0$ and the operator $\hat{\Lambda}^2 = -\hat{\Lambda}_0^2 + \mathcal{W}_\xi(\chi)$ consists of the Laplacian

$$\hat{\Lambda}_0^2 = \frac{\partial^2}{\partial\chi^2} + 4\cot(2\chi)\frac{\partial}{\partial\chi} - \frac{\hat{\ell}^2}{\sin^2(\chi)} - \frac{\hat{L}^2}{\cos^2(\chi)} \quad \text{(A2)}$$

on the six-dimensional hypersphere with the relative $\hat{\ell}^2$ and c.m. $\hat{L}^2$ orbital angular momentum operators, and the potential

$$\mathcal{W}_\xi(\chi) = \frac{2\xi^3\xi_0}{a_{\rm ho}^4}\left[1 - \frac{2 + \sin^2(2|\frac{\pi}{4} - \chi|)}{3\cos(\frac{\pi}{4} - |\frac{\pi}{4} - \chi|)}\right] \quad \text{(A3)}$$

with the characteristic length $a_{\rm ho} \equiv \sqrt{\hbar/(m\omega)}$ of the shell-shaped trapping potential $V_0(\boldsymbol{r})$, defining also the shell width.

The last term in Eq. (A1)

$$\mathcal{V}_c = -m\omega^2\xi\xi_0\sum_{l=1}^{\infty}\frac{\sin^{2l}(\frac{\pi}{4} - |\chi - \frac{\pi}{4}|)}{\cos^{2l+1}(\frac{\pi}{4} - |\chi - \frac{\pi}{4}|)}\left[\frac{\sin^2(\frac{\pi}{4} - |\chi - \frac{\pi}{4}|)}{4l+3} - \frac{\cos^2(\frac{\pi}{4} - |\chi - \frac{\pi}{4}|)}{4l-1}\right]\frac{4\pi}{4l+1}\sum_{\mu=-2l}^{2l} Y_{2l,\mu}(\theta,\phi)Y^*_{2l,\mu}(\Theta,\Phi), \quad \text{(A4)}$$

with $Y_{l,m}$ being the spherical harmonics on the three-dimensional sphere, couples all degrees of freedom.

Further, the boundary conditions, Eqs. (1a) and (1b), take a simpler form in hyperspherical coordinates:

$$\frac{1}{\sin(2\chi)\Psi}\frac{\mathrm{d}}{\mathrm{d}\chi}[\sin(2\chi)\Psi]|_{\chi\to 0} = -\frac{\sqrt{2}\xi}{a_0} \quad \text{for } \ell = 0, \quad \text{(A5a)}$$

$$\sin(2\chi)\Psi|_{\chi\to 0} = 0 \quad \text{for } \ell > 0. \quad \text{(A5b)}$$

When we neglect the coupling term $\mathcal{V}_c$, the angular variables of the relative (θ and ϕ) and c.m. (Θ and Φ) motions can be separated from each other as well as from the hyperradius ξ and hyperangle χ both in the Hamiltonian, Eq. (A1), and the boundary conditions, Eq. (A5a) and (A5b). In this way, the Hamiltonian Eq. (A1) would have the form of a spherically symmetric six-dimensional radially shifted harmonic oscillator, if the operator $\hat{\Lambda}^2$ and the boundary condition, Eq. (A5a), were ξ independent. However, this is not the case and we have to use a proper scheme to solve the reduced two-dimensional Schrödinger equation numerically. This is done approximately [48] within the adiabatic approximation. Namely, we first compute the eigenvalues $\lambda(n_\chi, L, \ell; \xi)$ and eigenfunctions $V_{n_\chi L\ell,\xi}(\chi)$ of the operator $\hat{\Lambda}^2$, taking into account Eq. (A5a) and (A5b), with ξ considered as a parameter. We then replace $\hat{\Lambda}^2$ in Eq. (A1) by λ, neglect the coupling $\mathcal{V}_c$ [53], and solve numerically the obtained eigenvalue equation for the hyperradial wave functions $U_{n_\xi n_\chi L\ell}(\xi)$ and the corresponding two-particle energies $E_{n_\xi n_\chi L\ell}$.

Appendix B: Transition from a 3D to 1D harmonic oscillator—At $r_0 = 0$ the two-body spectrum is exactly given by the spectrum of a 3D harmonic oscillator, $E_{n_\xi n_\chi} = [\mathcal{E}_{n_\chi}(a_0) + 2n_\xi + 3/2]\hbar\omega$, shifted by the dimensionless energies $\mathcal{E}_{n_\chi}$ of the hyperangular motion. The latter is reduced to the relative motion for $r_0 = 0$. The energies $\mathcal{E}_{n_\chi}$ are given by the roots of the equation [41]:

$$\sqrt{2}\frac{\Gamma(3/4 - \mathcal{E}_{n_\chi}/2)}{\Gamma(1/4 - \mathcal{E}_{n_\chi}/2)} = -\frac{a_{\rm ho}}{a_0}, \quad \text{(B1)}$$

where $\Gamma(z)$ is the Gamma function.

For $0 < a_0/a_{\rm ho} < 1$ and $n_\chi = 0$, we have derived

$$\mathcal{E}_0 = -(a_{\rm ho}/a_0)^2 + (1/8)(a_0/a_{\rm ho})^2 + O[(a_0/a_{\rm ho})^6]. \quad \text{(B2)}$$

However, for $r_0 \gg a_{\rm ho}$, the bound-state energies feature the spectrum of the 1D harmonic oscillator [48], $E_{n_\xi 0} \approx [\mathcal{E}_0(a_0) + n_\xi + 1/2]\hbar\omega$, where

$$\mathcal{E}_0 = -(a_{\rm ho}/a_0)^2 + (1/24)(a_0/a_{\rm ho})^2 + O[(a_0/a_{\rm ho})^6], \quad \text{(B3)}$$

valid for $0 < a_0/a_{\rm ho} < 1$.